Metasurface-enhanced photochemical activity in visible light absorbing semiconductors **©**⊘

Special Collection: Festschrift in honor of Louis E. Brus

Yamuna Paudel; Diego J. Chachayma-Farfan; Andrea Alù 🗓 ; Matthew Y. Sfeir 🗷 🗓



J. Chem. Phys. 160, 144710 (2024) https://doi.org/10.1063/5.0199589









Metasurface-enhanced photochemical activity in visible light absorbing semiconductors @

Cite as: J. Chem. Phys. 160, 144710 (2024); doi: 10.1063/5.0199589 Submitted: 23 January 2024 • Accepted: 25 March 2024 •







Published Online: 15 April 2024

Yamuna Paudel, ^{1,2} Diego J. Chachayma-Farfan, ^{1,3} Andrea Alù, ^{1,2,3} D and Matthew Y. Sfeir ^{1,2,a)} D



AFFILIATIONS

- ¹ Photonics Initiative, Advanced Science Research Center, City University of New York, New York, New York 10031, USA
- ²Physics Department, CUNY Graduate Center, City University of New York, New York, New York 10016, USA
- Department of Electrical and Computer Engineering, The University of Texas at Austin, Austin, Texas 78712, USA

Note: This paper is part of the JCP Festschrift in honor of Louis E. Brus.

a) Author to whom correspondence should be addressed: msfeir@gc.cuny.edu

ABSTRACT

Heterogeneous photocatalysis is an important research problem relevant to a variety of sustainable energy technologies. However, obtaining high photocatalytic efficiency from visible light absorbing semiconductors is challenging due to a combination of weak absorption, transport losses, and low activity. Aspects of this problem have been addressed by multilayer approaches, which provide a general scheme for engineering surface reactivity and stability independent of electronic considerations. However, an analogous broad framework for optimizing light-matter interactions has not yet been demonstrated. Here, we establish a photonic approach using semiconductor metasurfaces that is highly effective in enhancing the photocatalytic activity of GaAs, a high-performance semiconductor with a near-infrared bandgap. Our engineered pillar arrays with heights of ~150 nm exhibit Mie resonances near 700 nm that result in near-unity absorption and exhibit a field profile that maximizes charge carrier generation near the solid-liquid interface, enabling short transport distances. Our hybrid metasurface photoanodes facilitate oxygen evolution and exhibit enhanced incident photon-to-current efficiencies that are ~22× larger than a corresponding thin film for resonant excitation and 3× larger for white light illumination. Key to these improvements is the preferential generation of photogenerated carriers near the semiconductor interface that results from the field enhancement profile of magnetic dipolar-type modes.

Published under an exclusive license by AIP Publishing. https://doi.org/10.1063/5.0199589

INTRODUCTION

Heterogeneous photocatalysis driven by visible light absorbing semiconductors represents an important fundamental science problem with implications for a broad range of applications in pollution remediation, solar fuels, and high value chemical synthesis. First introduced in 1972 by Honda and Fujishima using ultraviolet illumination of TiO₂ to split water,² its extension to semiconductors with strong light visible absorption remains a major challenge. A wide variety of materials have been explored in this context, including II-VI semiconductors such as CdTe, III-V semiconductors such as GaP, higher-order compounds such as bismuth vanadate and oxynitride solid solutions, as well as two-dimensional materials including transition metal dichalcogenides.^{3–9} A key limitation is that there exists a large parameter space for optimization that must satisfy strict constraints on the bandgap energy, band alignments,

carrier mobility, corrosion resistance, and surface reactivity of the semiconductor. 10-13 As a result of these factors, as well as concerns related to cost and ease of fabrication, several other potential candidate materials with appropriate bandgaps have been less widely explored. 12,14,15 Simultaneously optimizing all the key processes has proved challenging as deficiencies in light absorption, charge transport, and chemical activity will all limit the overall photochemical efficiency. Furthermore, in a monolithic material, these factors are interrelated, which frequently makes it difficult to identify major loss pathways.

One particularly successful approach to address this optimization challenge has been to use multilayer schemes to decouple critical functionality. For example, ultrathin (~1 nm) surface layers have been employed to render the surface activity independent of the electronic properties of the semiconductor. Since its first demonstration, 16 a wide variety of semiconductor/surface layer combinations have been shown to exhibit enhanced surface catalytic activity and/or stability. Importantly, this approach has enabled the use of semiconductors that would otherwise be unfeasible because of poor activity and/or stability. 17-19 An important remaining challenge concerns the development of analogous schemes to engineer the absorbing properties of the semiconductor independent of its electronic structure and surface properties. Compared to UV photons, absorption of visible light tends to be weaker with a longer characteristic absorption length. This results in either less photons absorbed overall or absorbed further from the solid-liquid interface, imposing additional requirements for high purity of the semiconductor material to minimize transport losses. Various nanoscale approaches have been introduced to engineer the semiconductor's absorption, but a general effective strategy is still lacking. 20,21 For example, quantum-confined semiconductor nanocrystals have enhanced absorption cross sections near the band edge but their large surface-to-volume ratios exacerbate the parasitic effects of lossy surface states.^{22,23} Alternatively, the use of antenna-like effects of plasmonic metal nanoparticles (MNPs) has been proposed to tailor electric fields in the vicinity of the semiconductor surface.²⁴ However, controlling the size and coverage of MNPs on the surface of the semiconductor is an additional materials science challenge. More critically, absorption losses in MNPs are high^{25,26} and schemes to directly capture the resulting hot electrons are highly controversial. As a result, a suitable material has not yet been identified that has the necessary properties for efficient heterogeneous photocatalysis driven by low energy photons.

We posit that a different approach to nanostructuring materials may be effective in enabling independent tuning of critical absorption length scales for visible light absorbing semiconductor photocatalysts. Our approach is based on dielectric metasurfaces composed of two-dimensional arrays of patterned semiconductors that are engineered to tailor and enhance light-matter interactions via geometric resonances.^{27–30} In dielectric metasurfaces, the electric field profile supports a dominant contribution from Mietype resonances distinct from the electric dipole (ED) resonance that dominates in plasmonic MNPs. 10,27,31-35 Importantly, these additional modes, which include magnetic dipolar (MD)-type resonances, result in electric field localization within the nanostructure. Furthermore, they experience much reduced losses and enhanced efficiencies compared to MNPs. Importantly, the strength of the Mie resonances can be further enhanced in multilayered structures that achieve hybridization between a metal and dielectric response. 25,36 For example, the alignment of ED and MD resonances has been associated with the concept of "perfect" absorption, in which reflection is nearly completely suppressed. This concept has been demonstrated in the context of optoelectronic applications³⁰ including terahertz antennas.^{25,37} More recently, perfect absorbers based on non-radiating anapole modes have been explored in the context of photocatalysis.38 However, little attention has been paid to optimizing both the strength and spatial profile of absorption in photocatalytic metasurfaces, with the explicit goal of concentrating charge carrier generation near the point of utilization to minimize recombination losses and enhance the overall conversion efficiencies.4

Here, we propose a strategy to optimize near-infrared (NIR)driven photocatalytic processes in dielectric metasurface electrodes with strong Mie resonances. In particular, we focus on photonic structures that enable strong light interactions due to large contributions from magnetic dipole terms [Fig. 1(a)]. ^{26,42} In contrast to other resonant modes that result in large absorption dominated by the fields in the interior of the nanostructure, ^{38–40} MD-type modes maximize the absorbed power near the solid–liquid interface, a key aspect for achieving the highest conversion efficiencies. We have validated this concept using gallium arsenide (GaAs), a technologically relevant III–V semiconductor with a NIR direct band gap of

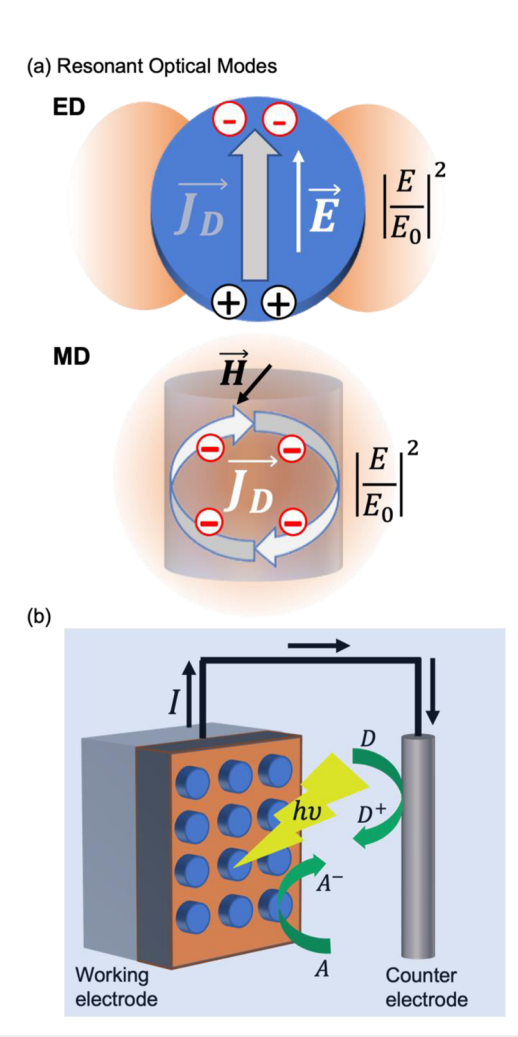


FIG. 1. Our photoelectrochemical device takes advantage of (a) resonant geometric modes to enhance the absorption of light in a semiconductor nanostructure. Top down view of a pillar showing the electric dipole (ED) modes excited by the electric field vector dominate in the absence of a geometrical resonance and result in the concentration of electromagnetic energy ($|E/E_0|^2$) in the near field of the cylinder (shaded region). Magnetic dipole (MD) modes excited by the magnetic field vector can also be resonantly enhanced in semiconductor metasurfaces resulting in circulating displacement currents (\overrightarrow{J}_D) that enhance the electric field within the cylinder. (b) We have designed semiconductor metasurfaces with strong MD resonances that function as working electrodes in an electrochemical device. Minority carriers reduce chemical species at the solid–liquid interface and a counter electrode

completes the electrochemical circuit.

~1.42 eV.⁴³ In this work, we show that a hybrid optical metasurface containing 150 nm pillars of n-type GaAs generates a strong absorption resonance near 700 nm that minimizes the optical reflectivity and maximizes absorption (>80%). When incorporated into an aqueous photoelectrochemical cell [Fig. 1(b)], the metasurface functions as a stable photoanode for oxygen evolution. Critically, our metasurface electrodes exhibit large photocurrent enhancements of more than 22× compared to the corresponding unpatterned thin film. Our analysis shows that this improvement results from the dual benefit of (1) enhancing the overall absorption in a thin layer of materials (relative to an unpatterned thin film) and (2) concentrating the spatial distribution of light near the surface of the semiconductor, reducing necessary diffusion lengths. These studies establish that photocatalytic applications will benefit from dielectric photonic structures generating tailored electric field patterns with low inherent losses.

RESULTS AND DISCUSSION

To achieve a high incident photon-to-current efficiency (IPCE) in heterogeneous catalytic applications, optimization of both the transport of carriers to a solid-liquid interface and their photochemical activity is required. 44,45 As in other optoelectronic devices, charge carrier migration is facilitated by a strong depletion field, which also helps suppress the recombination of photogenerated minority carriers. Photogenerated carriers outside of the depletion region will instead experience diffusive transport and be subject to typical bulk recombination processes. The consequence of losses during diffusive transport on the activity of different semiconductor photocatalysts is an important outstanding question. For example, it has been previously shown that significant losses occur during transport due to the presence of defects and dopants, which also reduce the width of the depletion region.⁴¹ As such, a key metric for estimating transport efficiency can be obtained by comparing two characteristic length scales: the absorption length corresponding to the evanescent decay of incident plane waves within the semiconductor (α^{-1}) and its depletion width (W_d) . The ratio $(\alpha W_d)^{-1}$ will generally become larger for longer wavelengths and higher background carrier densities, and significant transport losses are likely to occur. For small $(\alpha W_d)^{-1}$, e.g., less than one, most light absorption will occur within the depletion region and transport efficiencies will be high. We have calculated these ratios for crystalline GaAs using the measured refractive indices (Fig. S1) and calculated depletion widths (supplementary material) assuming a planar interface (Fig. 2). We find that $(\alpha W_d)^{-1}$ is greater than one, i.e., significant transport losses will occur, for red-NIR absorption near the band edge in materials in which the background carrier density exceeds 10¹⁷ cm⁻³. For example, at a doping level of 10¹⁸ cm⁻³ that is typical for commercially available GaAs wafers, a small $(\alpha W_d)^{-1}$ ratio is obtained only for wavelengths shorter than 500 nm [Fig. 2(b)]. At longer wavelengths (e.g., 700 nm), the absorption length is $\sim 34 \times$ the depletion width [Fig. 2(c)] such that carriers will be inefficiently harvested. This simple model captures the essence of the problem we aim to address: that in the absence of an alternative strategy for changing the distribution of photogenerated carriers, there are very stringent requirements on the quality of materials needed for photoelectrochemical (PEC) applications. We note that the width

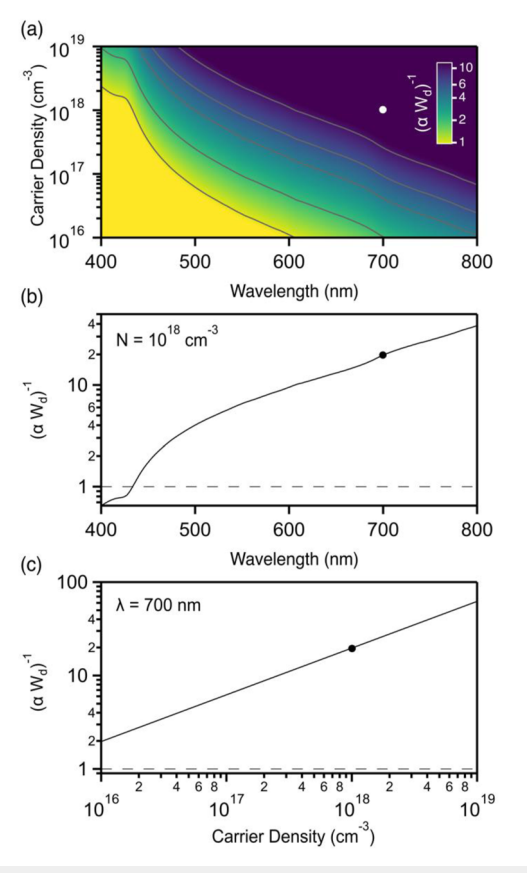


FIG. 2. The transport efficiency in a photoelectrochemical device can be approximated by the relative magnitude of the absorption length (α^{-1}) to the depletion width (W_d) . (a) This ratio is plotted for a semiconductor–water interface as a function of the majority carrier density of the semiconductor. Ratios of $(\alpha W_d)^{-1}$ less than or equal to one (red shading) correspond to efficient minority charge carrier transport. The transport efficiency will drop significantly for ratios greater than one (white shaded region). (b) A plot of $(\alpha W_d)^{-1}$ as a function of the incident wavelength of light for a semiconductor with $n \sim 3 \times 10^{18}$. At 700 nm $(\alpha W_d)^{-1}$ is $\sim 34 \times$. (c) A plot of $(\alpha W_d)^{-1}$ as a function of the carrier concentration for illumination at 700 nm. In all plots, the black dot indicates the material used in this study, which has a carrier density of $n \sim 3 \times 10^{18}$ cm $^{-3}$ and a resonant mode near 700 nm.

of the depletion region in a cylinder is always longer than a film as long as $W_d < R$ where R is radius of cylinder, corresponding to $N_D > 1 \times 10^{17}~{\rm cm}^{-3}.^{46}$ However, at the experimental doping level using in this study ($N_D = 3 \times 1018~{\rm cm}^{-3}$), the value of the cylindrical depletion width ($W_d = 13~{\rm nm}$) is nearly equivalent to the planar value (supplementary material Sect. B). As a result, only approximately 27% of the cross-sectional area of our cylindrical meta-atoms is depleted. As such, an approach based on tailoring the electric field profile within the semiconductor using photonic resonances has the potential to materially impact the photocatalytic efficiency of common semiconductor materials.

Our photocatalytic metasurfaces were designed to exhibit strong absorption resulting from the combination of electric and magnetic Mie resonances tuned to photon energies larger than the bulk GaAs bandgap (>1.4 eV). ^{26,42} In addition to supporting

a bandgap that is optimally matched to the solar spectrum, GaAs exhibits a high electron mobility and can support a wide doping range for optoelectronic applications. Still, its relatively weak absorption near the band edge and the relatively large cost to grow thick layers with high purity have limited its application to a few specialized technologies. In an individual subwavelength dielectric nanoparticle, resonance with a magnetic dipole mode occurs for the condition $\lambda/n = 2R$ where λ is the wavelength of light, n is index of refraction, and R is radius of nanoparticle. 26 We chose to optimize our system for a wavelength near 700 nm, which corresponds to a radius of ~90 nm. This wavelength is centered far enough above the bandgap so that optical absorption will occur over a broad optical resonance while still minimizing thermalization losses. To extend this concept to photocatalytic metasurfaces, we implemented a design consisting of square lattice of right cylinders capable of generating both electric and magnetic resonances.⁴⁷ Constant spacings in the in-plane (x, y) directions are used so that the optical response is polarization independent. To identify the contribution of resonant modes to the pillars array, we used finite-difference time-domain methods (Ansys Lumerical FDTD) to calculate the absorption, reflection, and electric field profiles.

To validate our designs, we fabricated both GaAs and Au/GaAs metasurfaces over a 300 μ m square array following the procedure outlined in the supplementary material with structural parameters that match the optimized structures determined using FDTD calculations. Briefly, metasurfaces were fabricated using electron beam lithography from silicon doped bulk GaAs wafers (University Wafer) with a (100) orientation [Fig. 4(a)]. An 80 nm silicon dioxide (SiO₂) mask is deposited using plasma enhanced chemical vapor deposition (PECVD) on clean substrates followed by a thick layer (~450 nm) of PMMA [Fig. 3(b)]. Following exposure and development of the PMMA [Figs. 3(c) and 3(d)], two different dry etching process are carried to transfer the pattern from photoresist to the

SiO₂ mask [Fig. 3(e)] and to etch GaAs [Fig. 3(f)]. This etchant is optimized to obtain both anisotropic sidewall and high selectivity. At this stage, GaAs metasurfaces are either cleaned to remove residual resist or further processed to fabricate hybrid Au/GaAs metasurfaces. For the latter, a 50 nm layer of Au is deposited using electron beam methods [Fig. 3(g)] followed by etching to remove the residual oxide layer from the top of the pillar [Fig. 3(h)]. This step ensures that metal only remains in the interstitials of the pillars, though we note that it results in a slightly tapered pillar. Scanning electron microscopy is used to verify our structures during each step of the process [Figs. 3(e)–3(h)]. Following previous reports, an ultrathin oxide layer (1 nm of Al₂O₃) is used to protect GaAs from corrosion during PEC operation and promote efficient water oxidation. 4,48,49

The optimal geometry for each structure was determined by sweeping the radius and pitch of the unit cell while monitoring the total absorption within the portion of the pillar that extends from the substrate [Figs. 4(a) and 4(e)]. This criterion is based on our expectation that carriers generated elsewhere in the structure will have negligible impact on the photocatalytic activity. Optimized structures have a radius of 90 nm and a pitch of 320 nm. An analysis of the optical response of these structures indicates significant contributions from Mie resonance enhanced surface absorption. The calculated absorption spectra of our optimized metasurfaces show strong absorption peaks near the design wavelength of 700 nm. For a design consisting of a pure GaAs metasurface, a single broad peak is observed, with the maximum absorption approaching 40% near 690 nm with tails stretching to the band edge at 880 nm [Fig. 4(c)]. In an alternative hybrid structure consisting of GaAs pillars with thin metal interstitial layer (Au/GaAs), the increase in magnitude of the maximum absorption to ~80% is accompanied by a narrowing of the resonance and slight blue shift to 675 nm [Fig. 4(f)]. The enhancement from the strong dielectric contrast between the metal substrate and dielectric nanostructure is consistent with previous studies.²⁵ In

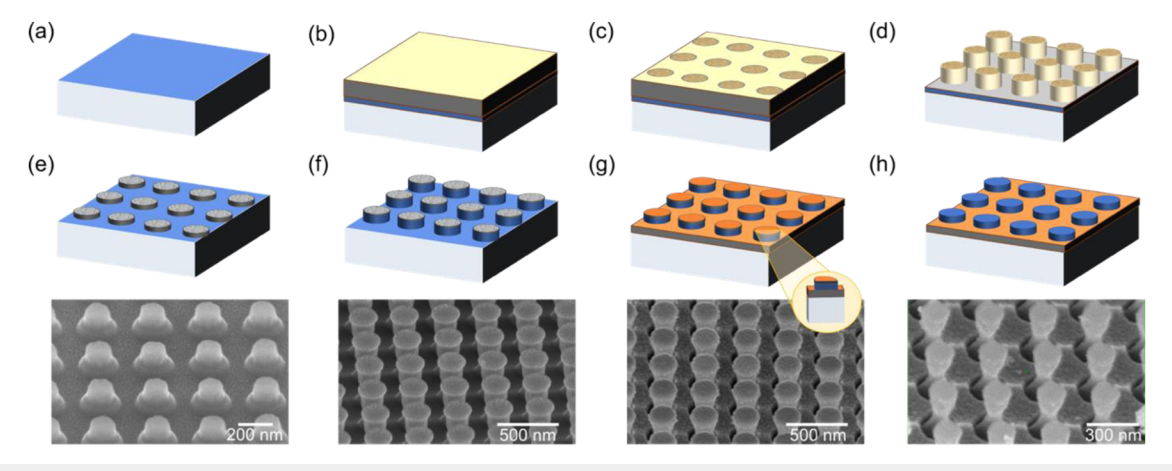


FIG. 3. Metasurface fabrication procedure. (a) GaAs film or wafer on which we deposit (b) 50 nm of silicon oxide and PMMA photoresist. (c) Electron beam lithography is used in a positive tone to expose the area outside of our circular pillar region followed by (d) development. (e) The resulting pattern is transferred to the silicon oxide hard mask using a reactive ion etching process. An SEM image of the resulting structure shows the silicon oxide disks plus some residual resist. (f) The pillar pattern is transferred to the GaAs film using inductive coupled plasma chlorine etching. SEM images show residual silicon oxide on top of the pillars. (g) For Au/GaAs metasurfaces, 50 nm of gold is deposited using electron beam evaporation, which can be seen in the accompanying SEM. (h) Wet etching is used to remove the residual layer of silicon oxide (GaAs metasurfaces) or silicon and gold (Au/GaAs metasurfaces) from the top of the pillars. The SEM image shows the final Au/GaAs metasurface. To protect the GaAs surface from corrosion, atomic layer deposition is used to conformally coat our structure with ~1 nm of aluminum oxide.

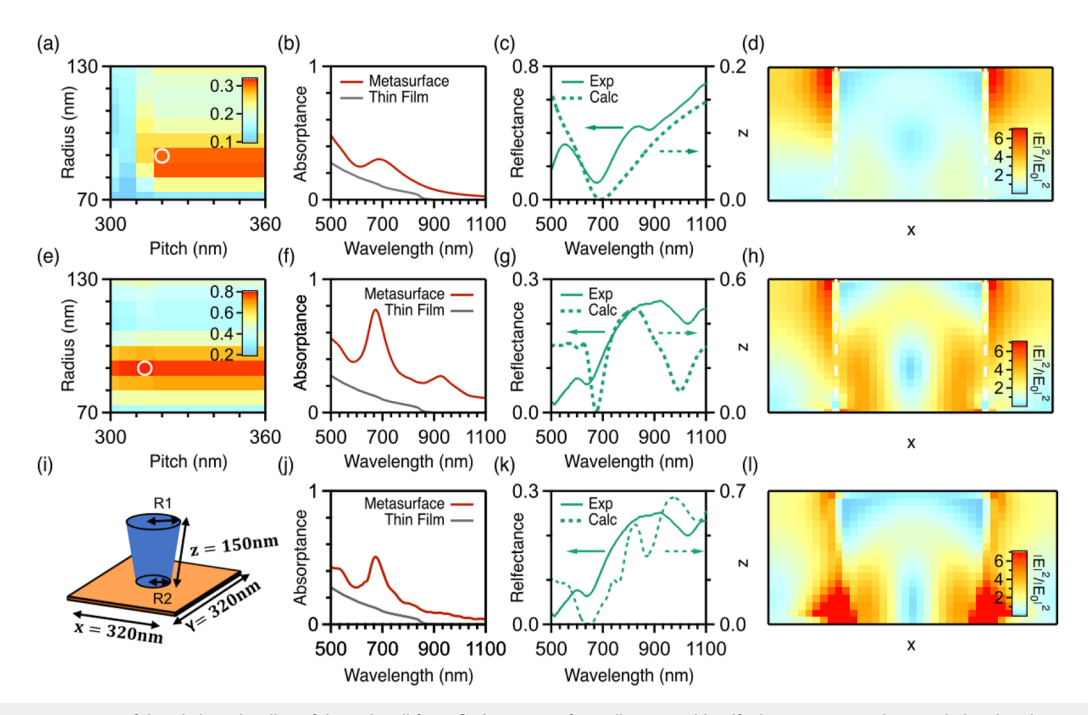


FIG. 4. (a) Parameter sweeps of the pitch and radius of the unit cell for a GaAs metasurface allow us to identify the parameters that maximize the absorptance at the target wavelength of 700 nm. The white circle indicates the parameters corresponding to our experimental geometry. (b) The calculated absorptance within our GaAs pillars at the optimized geometry shows a broad resonance peaked near 700 nm (solid green curve). The resonant enhancement of the absorption can be visualized by comparison to an equivalent thin film of the material with the same cross-sectional area (solid gray line). (c) The position of our resonances is verified by comparing the measured reflectivity (sold green line, left axis) to the calculated reflectivity (dashed green line, right axis). Good agreement of the reflection minimum is observed. (d) Cross-sectional image of the field enhancement within the xz plane of a GaAs pillar. Here, the x axis corresponds to the surface of the substrate and the white dashed lines indicate the air/GaAs boundary of the pillar. Panels [(e)–(h)] show the same data as [(a)–(d)] for the Au/GaAs metasurface. The major differences between the two are a stronger resonant absorption at 700 nm corresponding to a larger field enhancement within the walls of the pillar. Panels [(i)–(l)] for tapered Au/GaAs metasurface. Final isotropic wet etch shrinks shape of cylinder and left it tapered with R1 = 90 nm and R2 = 70 nm. (i) Schematic diagram for final fabricated Au/GaAs as shown in Fig. 4(h). (j) Optical absorptance for tapered cylinder and (k) and (l) are corresponding optical reflectivity and electric field enhancement.

addition, we observe a second resonant peak near 950 nm. Since this peak occurs for photon energies below the bandgap of GaAs, it represents in-plane scattering losses (analogous to a Wood's anomaly) that do not impact its photochemical activity. We can estimate the contributions of the increase in absorption in the metasurface by comparing these calculated spectra to the absorption of an equivalent volume of GaAs material whose light–matter interactions are determined by its bulk optical constants. We find that peak absorption of the GaAs metasurface is enhanced by a factor of \sim 3 while resonant absorption in the hybrid Au/GaAs metasurface is enhanced by a factor of 6 [Figs. 4(b) and 4(f)]. We note that calculations of tapered structures, with a structure geometry [Fig. 4(i)] designed to match Fig. 3(h), indicate a slightly broadening resonance with lower peak absorption [Fig. 4(j)].

In addition to an absorption increase, we expect that photocatalytic processes will be further impacted by the modified spatial distribution of photogenerated charge carriers in the photonic mode. As discussed above, carriers generated near the interface, particularly within the surface depletion region, will give the largest contribution to interfacial processes while carriers generated far from the interface will experience greater parasitic losses. To examine the resonant absorption modes, we calculated the magnitude of the field enhancement $|E|^2/|E_0|^2$ near the absorption maximum for

both GaAs and Au/GaAs metasurfaces. In Figs. 4(d) and 4(h), we show plot a cross section of our unit cell in the x-z plane that extends through the center of the pillar at x = y = 0 for light polarized along the y direction. The boundaries of the pillar are denoted by the dashed lines as well as the top and bottom of the graph. For both metasurface designs, we observe a large field concentration near the external walls of pillar that is reminiscent of an electric dipole mode. As the field is largely enhanced outside the semiconductor, we expect its effect on the photocatalytic efficiency to be minimal. However, we observe strong contributions from a mode with the electric field distributed radially within the dielectric pillar with its maximum near the interface and a minimum near the pillar's geometric center, as would be expected from a magnetic dipole resonance. Though the spatial mode is similar in both metasurface designs, its relative intensity is much higher in ms-Au/GaAs $(|E|^2/|E_0|^2 > 4 \text{ within the pillar) than in ms-GaAs } (|E|^2/|E_0|^2 < 1.5)$ within the pillar). Importantly for our studies, the maximum of the field intensity inside the pillar is unchanged near the sidewalls for tapered structures [Fig. 4(1)]. As the degree of tapering varies within and between samples, we carry out our subsequent analysis assuming straight sidewalls. These results suggest that while both ED and MD Mie resonant modes are excited near 700 nm, the MD mode is expected to preferentially enhance the IPCE.

To characterize the experimental optical resonances, we compare the calculated and experimental reflectivity spectra [Figs. 4(c), 4(g), and 4(k)] since a direct determination of the pillar absorption is difficult. An optical microscope was used to ensure that the experimental reflectivity spectra were collected only from the patterned region of our sample. The calculated reflectivity spectra show strong dips corresponding to the absorption maximum that reflect the spectral location of the resonant modes. The experimental resonances are in good agreement with the calculations, showing a reflection minimum near 680 nm for GaAs and near 640 nm for Au/GaAs. Similarly, we find that both calculation and experiment show that resonance near 700 nm is dispersionless. The lack of dependence on the incident angle of light (supplementary material, Sec. F) distinguishes the observed Mie mode from a diffraction effect. As in the calculation, a second strong sub-bandgap scattering mode near 1030 nm is observed for Au/GaAs. While the sharp minima of the reflectivity spectra show that reflection is nearly suppressed on resonance (minimum near 14%) as shown in Fig. 4(g), the offresonance reflectivity is lower than the calculation. This discrepancy is explained by the much larger range of incident angles in the experimental spectra (numerical aperture of 0.5), as well as a finite amount of inhomogeneity and deviations from the ideal calculated structures.

In a photoelectrochemical cell, we find that photocatalytic metasurfaces exhibit enhanced incident photon-to-current efficiencies (IPCEs) that significantly exceed the gain expected based on considering only enhancements in the magnitude of absorption. To quantify the IPCE, photoelectrochemical measurements were done using a standard three-electrode arrangement with the semiconductor as the working electrode. A Teflon mask was fabricated to match the active area of the metasurfaces $(1.64 \times 10^{-4} \text{ cm}^2)$ to ensure that only the patterned area contributes to the measured photocurrent. A similar mask with an area of 4.91×10^{-2} cm² is used with an unpatterned GaAs substrate for control experiments. We note that unlike GaAs substrates are thick compared to the absorption length for all wavelengths above the bandgap of the material. As such, the total absorption is limited by Fresnel reflection losses only and exceeds 65% at the relevant wavelengths. As such, there are minor differences in the total absorption between the flat film and the metasurfaces. Similarly, the surface area of the semiconductor in our Au/GaAs metasurface is nearly identical to that of the flat film. As a result, differences in the measured photocurrent between the flat film and the metasurfaces reflect differences in the spatial distributions of charge

Linear sweep voltammetry in a 1 M KCl aqueous electrolyte solution was used to measure the current between the working electrode and the silver/silver chloride reference electrode. Under illumination, the n-type semiconductor acts as a photoanode, generating oxygen via the water splitting reaction that resulted in the formation of bubbles. To distinguish resonant and nonresonant contributions to the overall IPCE, we employ two different light sources. A halogen lamp with visible and near-infrared emission was used to measure the broadband response, including both resonant and nonresonant contributions, of our PEC device. The overall spectral irradiance of this source is qualitatively similar to the reference air mass 1.5 spectra of sunlight [Fig. 5(a)] with an overall irradiance of ~7 suns (7130 W/m²). To isolate the photocurrent signal generated from resonant contributions, we use a single frequency laser

diode operating at 730 nm with a total irradiance of 5500 W/m². This excitation wavelength is chosen to compensate for the estimated solvent driven redshift of the dominant absorption peak of the metasurface.

Our metasurface electrodes show strong resonant enhancement of the magnitude of the IPCE. We find that metasurface fabrication has minimal effect on the flat band potential of the semiconductor, exhibiting a nearly identical $V_{oc} \approx -350$ mV for both pillars and substrates. This implies that the electrochemical properties are largely determined by the electronic structure of the parent GaAs material. However, we observe large differences in the photoelectrochemical response between the metasurface electrode and the flat electrode under illumination. Under resonant excitation at 730 nm and short circuit conditions [Fig. 5(b)], the hybrid Au/GaAs metasurface electrode exhibits $I_{SC}=113$ mA/cm² compared to 38 mA/cm² for the GaAs metasurface and 5 mA/cm² for the flat substrate (Table I). In all cases, the dark current is much less than the measured photocurrent (Fig. S3). Importantly, these measured resonant enhancement

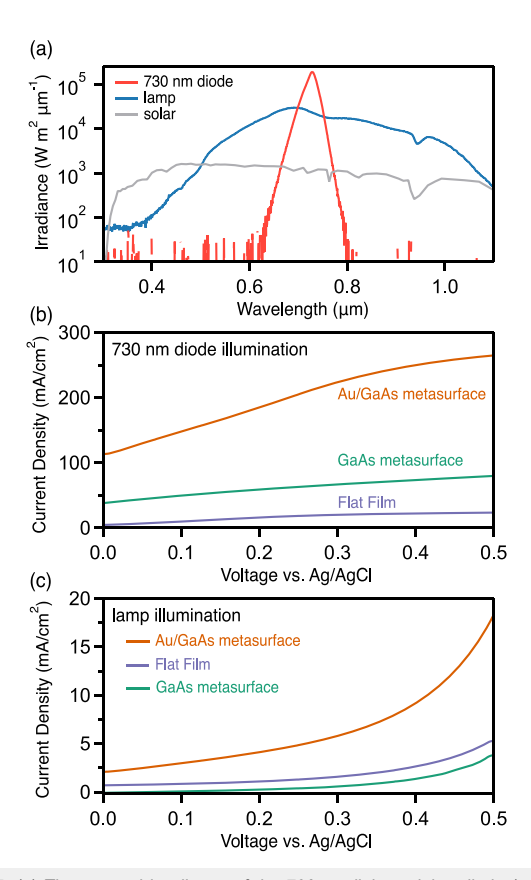


FIG. 5. (a) The spectral irradiance of the 730 nm light emitting diode (red) and lamp (blue) sources used for photoelectrochemical testing compared to the solar spectral irradiance (gray). The total irradiance for these sources is 5500, 7130, and 1000 W m $^{-2}$, respectively. (b) Under resonant illumination at 730 nm, significant photocurrent enhancement is observed in the metasurfaces compared to the thin film control sample. (c) For white light illumination consisting of primarily nonresonant wavelengths, the photocurrent generated in the GaAs metasurface is comparable to the thin film control. The Au/GaAs metasurface still exhibits a total photocurrent enhancement at a 0.5 V bias of $\sim 3.1 \times$.

TABLE I. Comparison of short circuit photocurrent (I_{SC}) values for GaAs films and metasurfaces.

	I_{SC} @730 nm (mA/cm ²)	I_{SC}/I_{SC} (GaAs film)@730 nm	I_{SC} @white light (mA/cm ²)	I_{SC}/I_{SC} (GaAs film)@white light
GaAs film	5	1	0.7	1
ms-GaAs	38	8	< 0.07	< 0.1
ms-Au/GaAs	11	22	2.2	3.1

effects of 22× for the Au/GaAs and 8× for the GaAs metasurface electrodes are significantly larger than the magnitudes expected if only the total absorption strength of the first 150 nm is considered $[\sim 8 \times \text{ and } 3 \times, \text{ respectively, as estimated from Figs. 4(f) and 4(j)}]$. As the measured photocurrent reflects the convolution of the probabilities for absorption and transport to the reactive interface, then our data suggest that additional factors need to be considered, such as the spatial mode of the field inside the electrode.

To test our hypothesis that the spatial profile of the electric field is critical to our overall enhancement gains, we compare resonant and broadband illumination under conditions that give the same net absorbed carrier density. As expected, the overall photocurrent generated in the metasurface under white light illumination is less than for single frequency excitation at 730 nm since it contains both resonant and nonresonant contributions. Under short circuit conditions for white light illumination, we measure $I_{SC} = 2.2 \text{ mA/cm}^2$ for the Au/GaAs metasurface compared to 0.7 mA/cm² for the unpatterned substrate under identical conditions (Table I). Importantly, this measurement allows us to estimate the impact of the narrower spatial distribution of photocarriers on resonance. As a simple test, we can compare the IPCE for different illumination conditions that yield the same photoexcited carrier density. Using the calculated absorption spectra [Fig. 4(f)] and correcting for differences in the spectral irradiance [Fig. 5(a)] between the two light sources, we find that the total rate of photogenerated carriers is approximately the same for 730 nm and white light excitation (Fig. S3). However, the short circuit current differs by a factor of ~22×. We conclude that the broadband illumination generates a large fraction of carriers outside the depletion region [Fig. 2(b)] that recombine before reaching the solid-liquid interface. A simplistic analysis of the band-flattening due to carrier accumulation supports our assertion that fundamentally different absorption profiles are obtained on resonance compared to broadband illumination (supplementary material).

CONCLUSION

Our results indicate that a properly designed metasurface can be highly beneficial for photocatalysis by both enhancing the total number of photogenerated carriers as well as tailoring their spatial distribution. We conclude that transport losses are significant for moderately doped semiconductors, such as those used in this study. As such, Mie resonances that concentrate absorption near a semiconductor interface, such as the one excited in our metasurfaces near 730 nm, will have an outsized effect on the overall IPCE enhancement factor. For example, the hybrid Au/GaAs metasurface shows an overall net IPCE enhancement under broadband illumination across the visible and NIR, in part because resonant IPCE enhancements are such a large contribution to the overall carrier generation (supplementary material). Notably, the GaAs metasurface exhibits a weaker resonant effect. As such, it exhibits a lower I_{SC} than the unpatterned film for broadband illumination, suggesting that resonant enhancement is not sufficient to overcome additional losses imparted for off-resonant excitation. As with other resonant nanostructures, it is possible to engineer and enhance the bandwidth of operation, and this represents one future direction for this research.

SUPPLEMENTARY MATERIAL

See the supplementary material for additional information and figures: measurements of the refractive index of GaAs; calculation of depletion widths; measurements of dark current; determination of absorbed carrier densities; additional schematics of meta-atoms; and alternative analysis of resonant contributions to the measured photocurrent.

ACKNOWLEDGMENTS

This work was supported by the donors of ACS Petroleum Research Fund under Grant No. 65743-ND6. A.A. and D.J.C. were partially supported by the Simons Foundation and the Air Force Office of Scientific Research. The authors acknowledge access to the facilities and research infrastructure of the Phase II NSF CREST Center IDEALS (Grant No. NSF-HRD-2112550). We thank Professor Maria Tamargo, Dr. Mingzhao Liu, and Candice Forrester for useful discussions. This research used the Nanofabrication core facility of the CUNY Advanced Science Research Center. This research used the Nanofabrication Facility and Materials Synthesis and Characterization Facility of the Center for Functional Nanomaterials (CFN), which is a U.S. Department of Energy Office of Science User Facility, at Brookhaven National Laboratory under Contract No. DE-SC0012704.

AUTHOR DECLARATIONS

Conflicts of Interest

The authors have no conflicts to disclose.

Author Contributions

Yamuna Paudel: Conceptualization (supporting); Formal analysis (lead); Investigation (lead); Methodology (lead); Visualization (equal); Writing - original draft (equal). Diego J. Chachayma-Farfan: Formal analysis (supporting); Investigation (supporting); Writing - review & editing (equal). Andrea Alù: Conceptualization (supporting); Formal analysis (supporting); Supervision (supporting); Writing - review & editing (equal). Matthew Y. Sfeir: Conceptualization (lead); Formal analysis (supporting); Funding acquisition (lead); Investigation (supporting); Methodology (supporting); Supervision (lead); Visualization (equal); Writing - original draft (equal).

DATA AVAILABILITY

The data that support the findings of this study are available from the corresponding author upon reasonable request.

REFERENCES

- ¹R. Li and C. Li, "Photocatalytic water splitting on semiconductor-based photocatalysts," in Advances in Catalysis (Elsevier, 2017), Vol. 60, pp. 1–57.
- ²A. Fujishima and K. Honda, "Electrochemical photolysis of water at a semiconductor electrode," Nature 238, 37 (1972).
- ³X. Gao, Y. Shen, Y. Ma, S. Wu, and Z. Zhou, "A water splitting photocatalysis: Blue phosphorus/g-GeC van der Waals heterostructure," Appl. Phys. Lett. 114,
- ⁴S. Hu, M. R. Shaner, J. A. Beardslee, M. Lichterman, B. S. Brunschwig, and N. S. Lewis, "Amorphous TiO2 coatings stabilize Si, GaAs, and GaP photoanodes for efficient water oxidation," Science 344, 1005 (2014).
- ⁵J. Gu, Y. Yan, J. L. Young, K. X. Steirer, N. R. Neale, and J. A. Turner, "Water reduction by a p-GaInP2 photoelectrode stabilized by an amorphous TiO2 coating and a molecular cobalt catalyst," Nat. Mater. 15, 456 (2016).
- $^{\bf 6}$ M. H. Lee $\it et al.,$ "p-Type InP nanopillar photocathodes for efficient solar-driven hydrogen production," Angew. Chem., Int. Ed. 51, 10760 (2012).
- ⁷M. T. McDowell, M. F. Lichterman, J. M. Spurgeon, S. Hu, I. D. Sharp, B. S. Brunschwig, and N. S. Lewis, "Improved stability of polycrystalline bismuth vanadate photoanodes by use of dual-layer thin TiO2/Ni coatings," J. Phys. Chem. C 118, 19618 (2014).
- ⁸J. A. Seabold and K.-S. Choi, "Efficient and stable photo-oxidation of water by a bismuth vanadate photoanode coupled with an iron oxyhydroxide oxygen evolution catalyst," J. Am. Chem. Soc. 134, 2186 (2012).
- ⁹C. Zhang, Y. Fan, X. Huang, K. H. L. Zhang, M. C. Beard, and Y. Yang, "Hotcarrier transfer at photocatalytic silicon/platinum interfaces," J. Chem. Phys. 152,
- ¹⁰W. Chen, X. Wang, J. Duan, C. Zhou, T. Liu, and S. Xiao, "Perfect absorption in free-standing GaAs nanocylinder arrays by degenerate critical coupling," Opt. Mater. 121, 111558 (2021).
- ¹¹W. S. Hobson and A. B. Ellis, "Photoluminescent properties of n-GaAs electrodes: Applications of the dead-layer model to photoelectrochemical cells," J. Appl. Phys. 54, 5956 (1983).
- ¹²P. A. Kohl and A. J. Bard, "Semiconductor electrodes: XVIII. Liquid junction photovoltaic cells based on n-GaAs electrodes and acetonitrile solutions," J. Electrochem. Soc. 126, 603 (1979).
- $^{\bf 13}$ R. N. Hall, G. E. Fenner, J. D. Kingsley, T. J. Soltys, and R. O. Carlson, "Coherent light emission from GaAs junctions," Phys. Rev. Lett. 9, 366 (1962).
- ¹⁴S. Hu, C.-Y. Chi, K. T. Fountaine, M. Yao, H. A. Atwater, P. Daniel Dapkus, N. S. Lewis, and C. Zhou, "Optical, electrical, and solar energy-conversion properties of gallium arsenide nanowire-array photoanodes," Energy Environ. Sci. 6, 1879 (2013).
- $^{15}\mathrm{G.}$ Siddiqi, Z. Pan, and S. Hu, "III–V semiconductor photoelectrodes," in Semiconductors and Semimetals (Elsevier, 2017), Vol. 97, pp. 81-138.
- 16 Y. W. Chen, J. D. Prange, S. Dühnen, Y. Park, M. Gunji, C. E. D. Chidsey, and P. C. McIntyre, "Atomic layer-deposited tunnel oxide stabilizes silicon photoanodes for water oxidation," Nat. Mater 10, 539 (2011).

- 17D. Lee, W. Wang, C. Zhou, X. Tong, M. Liu, G. Galli, and K.-S. Choi, "The impact of surface composition on the interfacial energetics and photoelectrochemical properties of BiVO₄," Nat. Energy 6, 287-294 (2021).
- ¹⁸T. W. Kim and K.-S. Choi, "Nanoporous BiVO₄ photoanodes with dual-layer oxygen evolution catalysts for solar water splitting," Science 343, 990 (2014).
- 19 K. Maeda, T. Takata, M. Hara, N. Saito, Y. Inoue, H. Kobayashi, and K. Domen, "GaN:ZnO solid solution as a photocatalyst for visible-light-driven overall water splitting," J. Am. Chem. Soc. 127, 8286 (2005).
- ²⁰ A. Ghobadi, T. G. Ulusoy Ghobadi, F. Karadas, and E. Ozbay, "Semiconductor thin film based metasurfaces and metamaterials for photovoltaic and photoelectrochemical water splitting applications," Adv. Opt. Mater. 7, 1900028 (2019).
- ²¹Y. Chen, W. Zheng, S. Murcia-López, F. Lv, J. R. Morante, L. Vayssieres, and C. Burda, "Light management in photoelectrochemical water splitting-From materials to device engineering," J. Mater. Chem. C 9, 3726 (2021).
- ²²J. Huang, Z. Huang, Y. Yang, H. Zhu, and T. Lian, "Multiple exciton dissociation in CdSe quantum dots by ultrafast electron transfer to adsorbed methylene blue," J. Am. Chem. Soc. 132, 4858 (2010).
- ²³Y. Yang, W. Rodríguez-Córdoba, and T. Lian, "Ultrafast charge separation and recombination dynamics in lead sulfide quantum dot-methylene blue complexes probed by electron and hole intraband transitions," J. Am. Chem. Soc. 133, 9246
- $^{\mathbf{24}}\mathrm{K}.$ Qian $\mathit{et~al.},$ "Surface plasmon-driven water reduction: Gold nanoparticle size matters," J. Am. Chem. Soc. 136, 9842 (2014).
- ²⁵D. Ray, T. V. Raziman, C. Santschi, D. Etezadi, H. Altug, and O. J. F. Martin, "Hybrid metal-dielectric metasurfaces for refractive index sensing," Nano Lett. 20,
- $^{\bf 26}$ A. I. Kuznetsov, A. E. Miroshnichenko, M. L. Brongersma, Y. S. Kivshar, and B. Luk'yanchuk, "Optically resonant dielectric nanostructures," Science 354, aag2472
- ²⁷N. I. Landy, S. Sajuyigbe, J. J. Mock, D. R. Smith, and W. J. Padilla, "Perfect metamaterial absorber," Phys. Rev. Lett. 100, 207402 (2008).
- ²⁸R. Alaee, M. Albooyeh, and C. Rockstuhl, "Theory of metasurface based perfect absorbers," J. Phys. D: Appl. Phys. 50, 503002 (2017).
- ²⁹D. G. Baranov, D. A. Zuev, S. I. Lepeshov, O. V. Kotov, A. E. Krasnok, A. B. Evlyukhin, and B. N. Chichkov, "All-dielectric nanophotonics: The quest for better materials and fabrication techniques," Optica 4, 814 (2017).
- 30 E. Cortés, F. J. Wendisch, L. Sortino, A. Mancini, S. Ezendam, S. Saris, L. de S Menezes, A. Tittl, H. Ren, and S. A. Maier, "Optical metasurfaces for energy conversion," Chem. Rev. 122, 15082 (2022).
- ³¹ F. A. Chaudhry, L. Escandell, E. López-Fraguas, R. Vergaz, J. M. Sánchez-Pena, and B. García-Cámara, "Light absorption enhancement in thin film GaAs solar cells using dielectric nanoparticles," Sci. Rep. 12, 9240 (2022).
- 32 L. Zhu, K. Liu, T. Hu, W. Dong, Z. Chen, and Z. Wang, "UV-visible photocurrent enhancement using metal-semiconductor-metal with symmetric and asymmetric double Schottky barriers," Nanoscale 10, 12848 (2018).
- 33 O. Mitrofanov, L. L. Hale, P. P. Vabishchevich, T. S. Luk, S. J. Addamane, J. L. Reno, and I. Brener, "Perfectly absorbing dielectric metasurfaces for photodetection," APL Photonics 5, 101304 (2020).
- ³⁴L. Hale, T. Siday, P. P. Vabishchevich, C. T. Harris, T. S. Luk, J. L. Reno, I. Brener, and O. Mitrofanov, "Efficient terahertz detection with perfectly-absorbing metasurface," in 2019 44th International Conference on Infrared, Millimeter, and Terahertz Waves (IRMMW-THz) (IEEE, Paris, France, 2019), pp. 1-2.
- 35 S. Liu, G. A. Keeler, J. L. Reno, M. B. Sinclair, and I. Brener, "III-V semiconductor nanoresonators—A new strategy for passive, active, and nonlinear all-dielectric metamaterials," Adv. Opt. Mater. 4, 1457 (2016).
- 36 B. Auguié and W. L. Barnes, "Collective resonances in gold nanoparticle arrays," Phys. Rev. Lett. 101, 143902 (2008).
- ³⁷S. Liu et al., "Resonantly enhanced second-harmonic generation using III-V semiconductor all-dielectric metasurfaces," Nano Lett. 16, 5426 (2016).
- 38 L. Hüttenhofer, M. Golibrzuch, O. Bienek, F. J. Wendisch, R. Lin, M. Becherer, I. D. Sharp, S. A. Maier, and E. Cortés, "Metasurface photoelectrodes for enhanced solar fuel generation," Adv. Energy Mater. 11, 2102877 (2021).

- ³⁹L. Hüttenhofer, F. Eckmann, A. Lauri, J. Cambiasso, E. Pensa, Y. Li, E. Cortés, I. D. Sharp, and S. A. Maier, "Anapole excitations in oxygen-vacancy-rich TiO_{2-x} nanoresonators: Tuning the absorption for photocatalysis in the visible spectrum," ACS Nano 14, 2456 (2020).
- ⁴⁰ S. J. Kim, I. Thomann, J. Park, J.-H. Kang, A. P. Vasudev, and M. L. Brongersma, "Light trapping for solar fuel generation with Mie resonances," Nano Lett. 14, 1446 (2014).
- ⁴¹K. Appavoo, M. Liu, C. T. Black, and M. Y. Sfeir, "Quantifying bulk and surface recombination processes in nanostructured water splitting photocatalysts via in situ ultrafast spectroscopy," Nano Lett. 15, 1076 (2015).
- 42 D. Neshev and I. Aharonovich, "Optical metasurfaces: New generation building blocks for multi-functional optics," Light Sci. Appl. 7, 58 (2018).
- ⁴³C. Kittel, *Introduction to Solid State Physics*, 8th ed. (Wiley, Hoboken, NJ, 2005).
- ⁴⁴Z. Chen, H. N. Dinh, and E. Miller, *Photoelectrochemical Water Splitting* (Springer New York, New York, NY, 2013).

- ⁴⁵F. R. F. Fan and A. J. Bard, "Semiconductor electrodes. 24. Behavior of photoelectrochemical cells based on p-type gallium arsenide in aqueous solutions," J. Am. Chem. Soc. **102**, 3677 (1980).
- ⁴⁶J. H. Luscombe and C. L. Frenzen, "Depletion lengths in semiconductor nanostructures," Solid-State Electron. 46, 885 (2002).
- ⁴⁷A. B. Evlyukhin, C. Reinhardt, and B. N. Chichkov, "Multipole light scattering by nonspherical nanoparticles in the discrete dipole approximation," Phys. Rev. B **84**, 235429 (2011).
- 48 J. Qiu, G. Zeng, M.-A. Ha, B. Hou, M. Mecklenburg, H. Shi, A. N. Alexandrova, and S. B. Cronin, "Microscopic study of atomic layer deposition of TiO₂ on GaAs and its photocatalytic application," Chem. Mater. **27**, 7977 (2015).
- $^{\mathbf{49}}$ J. Qiu, G. Zeng, M. Ge, S. Arab, M. Mecklenburg, B. Hou, C. Shen, A. V. Benderskii, and S. B. Cronin, "Correlation of Ti³+ states with photocatalytic enhancement in TiO2-passivated p-GaAs," J. Catal. 337, 133 (2016).